JOURNAL OF GEOPHYSICAL RESEARCH, VOL. 101, NO. C3, PAGES 6651–6667, MARCH 15, 1996

Coastal ocean fronts and eddies imaged with ERS 1 synthetic aperture radar

J. A. Johannessen,[1,2] R. A. Shuchman,[3] G. Digranes,[1] D. R. Lyzenga,[3]
C. Wackerman,[3] O. M. Johannessen,[4] and P. W. Vachon[5]

Abstract. ERS 1 C band synthetic aperture radar (SAR) data were collected during the Norwegian Continental Shelf Experiment (NORCSEX) both in November 1991 during the ERS 1 commissioning phase and at different seasons in 1992 and 1993. Characteristic SAR image expressions are observed in relation to perturbation of the surface current–short wave interaction across the Norwegian Coastal Current front for winds less than 10–12 m s^{-1}. In situ measurements document the existence of alternating zones of convergence and divergence coexisting with a strong near-surface current shear of nearly $4f$ (where f is the Coriolis parameter) across a distance of a few kilometers. Under calm to moderate winds, i.e., 4–7 m s^{-1}, characteristic expressions of upper ocean circulation features also include the manifestation of eddies through the presence of surface film which damps the Bragg waves. Comparison of a near-coincident National Oceanic and Atmospheric Administration advanced very high resolution radiometer image and an ERS 1 SAR image supports the interpretation that surface current fronts are imaged by SAR. In combination with an SAR image simulation model, the relative quantitative importance of shear, convergence, and divergence along the front is examined. Although the model formulation is simple and the absolute magnitude of the perturbations is uncertain, the study shows that the SAR images can sometimes be used to interpret frontal dynamics, including growth and decay of meanders.

1. Introduction

The marine coastal environment is characterized by the interaction of a complex set of upper ocean and atmospheric boundary layer processes having spatial and temporal scales ranging from meters to hundred of kilometers and seconds to several days. These processes and their interactions are not always well understood, primarily because of the difficulties involved in making in situ observations at the proper spatial and temporal scales. Consequently, mesoscale ocean circulation models are often incompletely validated. Because of the wide range of scales involved, remote sensing can play a valuable role in monitoring the marine coastal environment and in validating circulation models. Hitherto, this role has been filled mostly by spaceborne infrared measurements of the sea surface temperature field, which allow frontal boundaries associated with mesoscale circulation patterns to be observed. However, this application is limited by frequent cloud cover along many coastal regions. There is therefore a need to develop observational methods using spaceborne microwave sensors such as high-resolution synthetic aperture radar (SAR) imaging systems.

Unlike infrared radiometers and visible imaging systems, the SAR is unaffected by cloud cover and visible light conditions, and unlike the radar altimeter, the SAR provides a two-dimensional image of the surface. SAR images from the ocean are principally formed by resonant Bragg scattering, whereby the transmitted radar waves are reflected back to the antenna by gravity waves of approximately the radar wavelength [*Wright*, 1978]. Spatial variations of these short waves are usually induced by larger-scale features and processes in the marine boundary layer. At incidence angles around 20° or so, specular reflection may also contribute to the radar backscatter [*Donelan and Pierson*, 1987]. However, the relatively large surface slopes required to produce specular reflections at these incidence angles are mostly associated with short surface waves (<1-m wavelengths), so the mechanisms which produce variations in this component are at least qualitatively similar to those involved in Bragg scattering. In particular, it is documented that long gravity waves, variable wind velocities and stratification in the marine atmospheric boundary layer, and variable currents associated with upper ocean circulation features can be imaged by SAR [*Hasselmann et al.*, 1985; *Beal et al.*, 1981; *Vesecky and Stewart*, 1982; *Alpers*, 1985; *Fu and Stewart*, 1983; *Fu and Holt*, 1982; *Johannessen et al.*, 1991]. Moreover, the presence of pollutant oil spill and natural slicks at the sea surface can be expressed as dark features in SAR images through the damping of gravity waves [*Krishen*, 1973; *Alpers and Huhnerfuss*, 1989].

Since the launch of the first European Space Agency (ESA) remote sensing satellite (ERS 1) in July 1991, documentation of the C band SAR imaging ability has advanced further [*European Space Agency*, 1993, 1994]. This paper provides an assessment of the ability of the vertical polarization, ERS 1 C band SAR in imaging of upper ocean circulation features such

[1]Nansen Environmental and Remote Sensing Center, Bergen, Norway.
[2]Now at European Space Agency, European Space Research and Technology Centre, Noordwijk, Netherlands.
[3]Environmental Research Institute of Michigan, Ann Arbor.
[4]Nansen Environmental and Remote Sensing Center, Geophysical Institute, University of Bergen, Bergen, Norway.
[5]Canada Centre for Remote Sensing, Ottawa, Ontario, Canada.

Paper number 95JC02962.
0148-0227/96/95JC-02962$05.00

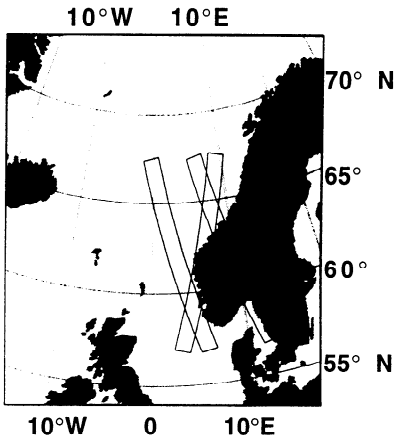

Figure 1a. Locations of ERS 1 synthetic aperture radar (SAR) ascending and descending tracks along the coast of Norway.

as coastal oceanic fronts and eddies. The primary objective is to improve the understanding of the complex modulation of the radar backscatter under a variety of ocean surface conditions and, in turn, provide better quantitative interpretations and subsequent application of the SAR images, in particular, for studies of frontal dynamics. A coastal zone with the persistent presence of a coastal current front was selected off the west coast of Norway [*Haugan et al.*, 1991]. Results from this Norwegian Continental Shelf Experiment (NORCSEX) are presented in section 2. In section 3 we present a simulation study of SAR image expressions which can lead to a new quantitative application of SAR images in coastal ocean circulation studies. A summary follows in section 4.

2. The Data

SAR images obtained along the coast of Norway between July 1991 and December 1993 are presented and discussed. Low-resolution (100 m) SAR images are routinely transmitted from the Tromsø Satellite Station (Norway) to Nansen Environmental and Remote Sensing Center (NERSC). At NERSC these data are processed and analyzed. During field campaigns, interpreted images are faxed to research vessels. This provides the ability to steer the ship into regions where the SAR images express interesting features. Synoptic in situ data, although not measured simultaneously, are valuable to validate the SAR imaging capabilities, enable improved interpretations of the images, and subsequently develop geophysical retrieval algorithms. In addition, standard meteorological observations from nearby coastal stations are useful.

2.1. The NORCSEX'91 Validation Study

During the commissioning phase from August 15 to December 15, 1991, ERS 1 orbited the Earth in a 3-day exact repeat cycle. In this period a large number of SAR images were regularly obtained along the west coast of Norway (Figure 1a) as part of an ESA calibration-validation campaign and NORCSEX'91 [*Attema*, 1992; *Johannessen et al.*, 1993a]. The field campaign during NORCSEX'91 was conducted from November 6 to 29, centered on the continental shelf surrounding Haltenbank (Figure 1b). The study was a continuation of NORCSEX'88 [*Johannessen et al.*, 1991], and it focused on the ERS 1 C band SAR imaging capabilities, in particular, investigating (1) how frontal boundaries associated with wind, current, and internal waves lead to characteristically different backscatter modulations that, in turn, can be distinguished and classified in SAR images; and (2) under what environmental conditions this classification is possible. Interpreted SAR data (usually between 3 and 24 hours after acquisition) were transferred to R/V *Håkon* Mosby, the University of Bergen research vessel, which was instrumented with a standard conductivity-temperature-depth (CTD) profiler, Seasoar, 150-kHz acoustic Doppler current profiler (ADCP), surface thermistor, and a standard meteorological station (about 10 m height). Temporal and spatial variations in the upper ocean currents, the atmospheric boundary layer stability, and the near-surface wind field were then continuously measured during and between SAR acquisitions. In particular, these ship measurements were conducted in locations where the SAR images expressed distinct features. In addition, six moorings, each with five current meters, were deployed about 50 km apart to monitor temporal variations in the current on the continental shelf and along the shelf break.

2.1.1. Oceanographic conditions. In general, the Norwegian Coastal Current (NCC) in the region (Figure 1b) is steered northeastward between the bank and the coast, while a weak anticyclonic flow of offshore Atlantic water usually appears to be trapped on the bank. In turn, a current front with cyclonic current shear is formed at the boundary between these two water masses [*Haugan et al.*, 1991]. Evidence of this is manifested in the temporal variations of the near-surface current obtained at the two current meter moorings located northwest (CM3) and southeast (CM4) of the front (Figure 2a) and in the spatial and temporal changes of the upper ocean current across the front obtained from the ship-mounted ADCP (Figure 2b). At mooring CM4 the maximum current reaches 1.25 m s^{-1}, while significant perturbations of 1 m s^{-1} in less than 6 hours are observed. The average semidiurnal tidal current in the region is about 0.10 m s^{-1}. The core of the NCC has a width of about 25 km, and the cyclonic current shear across the front (along the ship track) reaches a maximum of about 0.5 ×

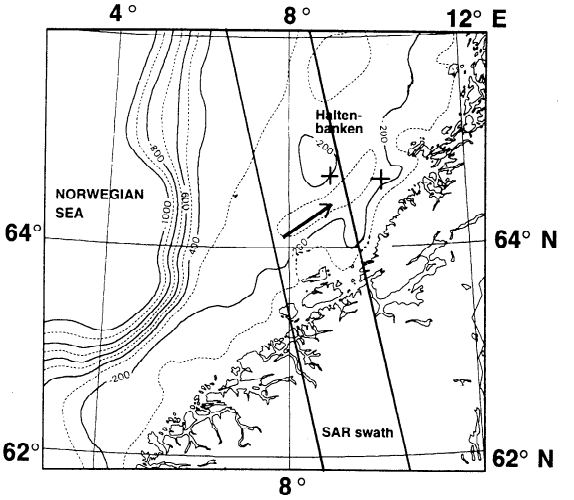

Figure 1b. Ascending SAR track across the Norwegian Continental Shelf Experiment 1991 (NORCSEX'91) experimental region superimposed on a bathymetric map. Current moorings CM3 (west) and CM4 (east) are marked with pluses, and the arrow indicates the mean location and direction of the Norwegian Coastal Current within the SAR swath.

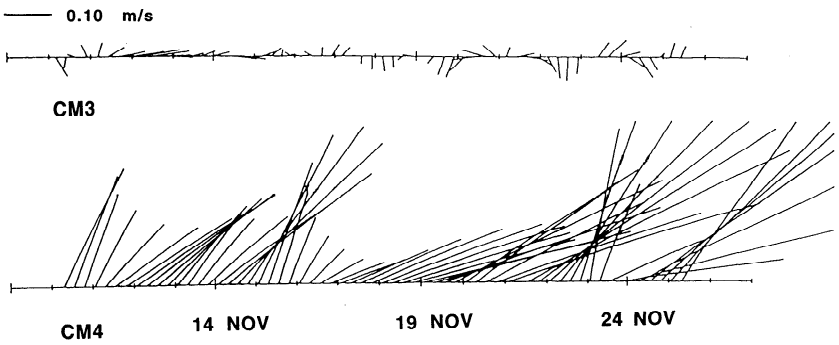

Figure 2a. Temporal variations in the current vectors at 25 m depth at CM3 and CM4 (locations marked in Figure 1b).

10^{-3} s^{-1} or nearly $4f$ (where f is the Coriolis parameter) over a distance of a few kilometers. Convergence is an order of magnitude smaller.

The ship transects across this frontal boundary between the bank and coastal islands were repeated three to four times during the field campaign. Although the current magnitude, the boundary position, and pattern and strength of convergence and divergence along the transects varied, the overall structure was maintained, i.e., a northeastward flowing NCC (in agreement with *Haugan et al.* [1991]) with a core width of 25 km (Figure 2c). In consideration of repeated SAR coverage of this region, one might therefore expect persistent frontal boundaries with a mean northeastward orientation to be present. The spatial distribution of the sea surface temperature field retrieved with the National Oceanic and Atmospheric Administration (NOAA) advanced very high resolution radiometer (AVHRR) satellite image on October 29, 1991 (the nearest cloud-free image in time), confirms this picture by the presence of a weak temperature front (Plate 1).

The vertical current structure across the front is shown in Figure 3, and the vertical temperature, salinity, and density structures obtained with the towed Seasoar are shown in Plate

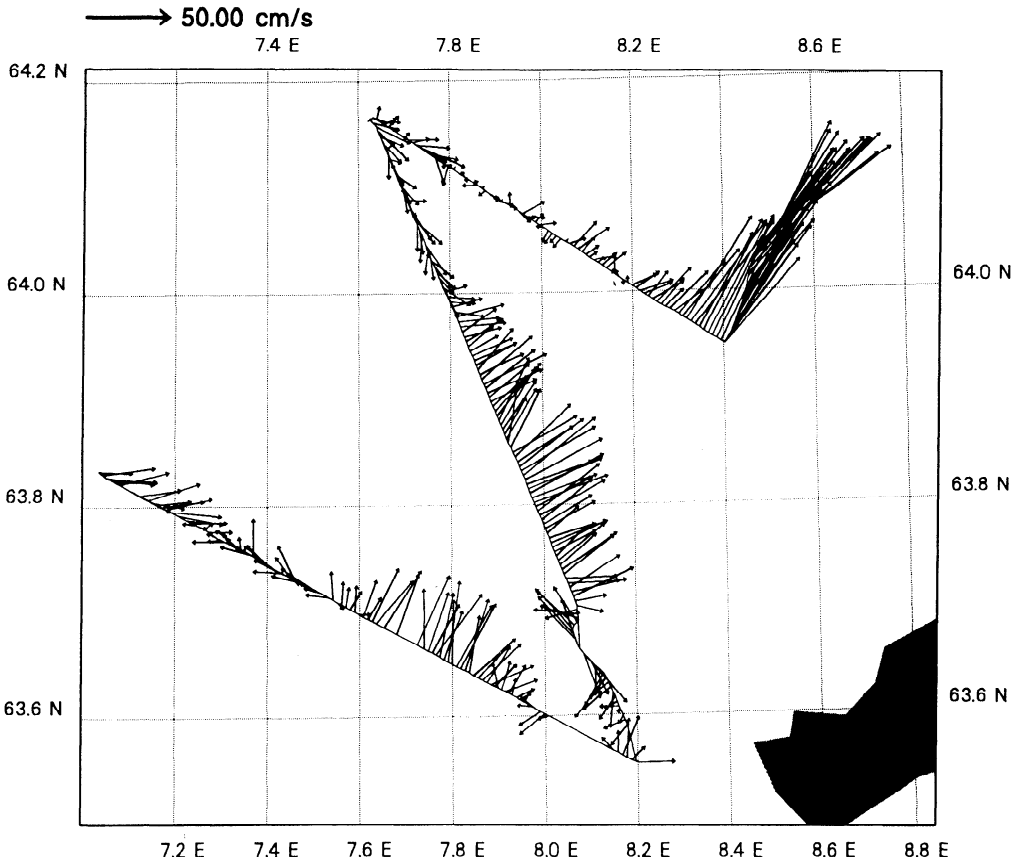

Figure 2b. Spatial (and temporal) variations in the current vector at 15 m depth obtained across the Norwegian Coastal Current with a ship-mounted 150-kHz acoustic Doppler current profiler on November 11. Each vector represent the average over 150 s, giving a spatial resolution of about 525 m at mean ship speed of 7 knots (3.5 m s^{-1}).

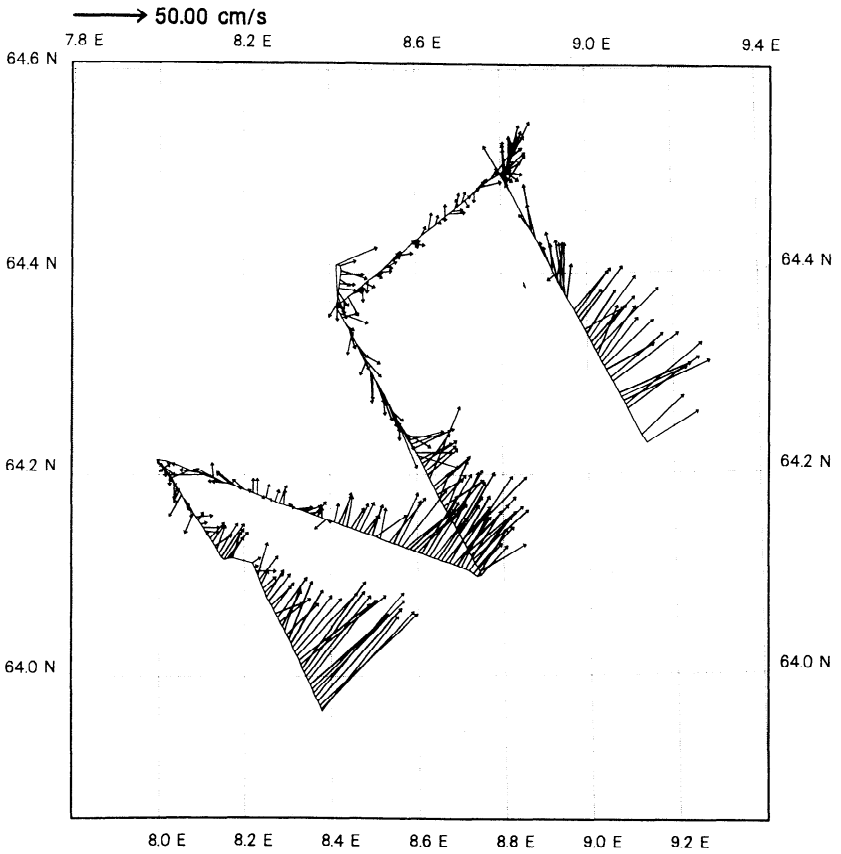

Figure 2c. Same as Figure 2b, but obtained on November 15–16.

2. The core of the NCC extends down to about 100 m, flowing in a mean northeastward direction. The characteristics of the NCC can be examined using the thermal wind relationship

$$\partial u/\partial z = (g/f\rho)\partial\rho/\partial n \quad (1)$$

where u is the horizontal (cross section) speed, g is gravitational acceleration, f is the Coriolis parameter, ρ is density, and n is direction along the section. A mean horizontal density gradient of 5.6×10^{-5} kg m^{-4} is obtained using a vertical shear of 4×10^{-3} s^{-1} as measured from the ADCP data. This agrees with the observed large-scale density gradient (27.1 to 25.8 over 25 km), suggesting that the NCC current is in near-geostrophic balance. A Rossby number ($Ro = U/fL$, where U is the mean current and L is the width of the current pattern) of order 10^{-1} lends further support to this assumption.

Within the NCC, on the other hand, the converging and diverging patterns in the current vectors reveal the presence of ageostrophic motion. The thermohaline and density structure show horizontal variations with a typical scale of 5 km in correspondence to this. In particular, the convergence zone found within the cyclonic shear coincides with a horizontal density gradient of about 1.1×10^{-4} kg m^{-4}, while the doming of isopycnals and isohalines found in the upper 50 m near the middle of the section leads to formation of a somewhat weaker surface front (i.e., 0.8×10^{-4} kg m^{-4}). The latter are collocated with the core of the surface current. The current vectors, moreover, indicate the existence of a zone of relatively strong convergence and divergence in the NCC nearshore, with a maximum strength of 0.5×10^{-3} s^{-1} over a few kilometers. In this region the corresponding salinity and density variations are less pronounced, since water of Atlantic origin is not present. The relatively minor sea surface temperature front, i.e., <1°C (in agreement with the IR image shown in Plate 1), as well as vertical temperature change imply that the baroclinic structure is maintained through the salinity field.

It is expected that the converging and diverging features as well as the strong persistent current shear zones depicted in the NCC are likely to show up in the SAR images. The frontal boundaries and their structural changes recognized in a sequence of SAR images in the 3-day repeat cycle may consequently reveal dynamic patterns along the current front.

2.1.2. SAR image expressions of fronts. In the sequence of 17 ascending SAR scenes obtained during NORCSEX'91, evidence of frontal boundaries is identified in five images or in 30% of the images, with maximum radiometric contrasts (peak to background) ranging from +3 to −2 dB. (In comparison, *Laur et al.* [1993] report that the radiometric stability and accuracy of ERS 1 SAR are both about 0.2 dB). The boundaries are inserted onto a geographic map in Figure 4a. During these five ascending SAR overpasses the wind speed remained between 4 and 10 m s^{-1}, while the boundary layer stratification remained between unstable (−3°C) to neutral. In comparison, the other 12 passes were obtained at winds exceeding 10–12 m s^{-1}, and in these cases the sea surface roughness was apparently dominated by the large-scale wind field.

As depicted in Figure 4a, the meandering fronts at scales from 10 to 50 km are mostly aligned in the mean northeastward direction of the current, with decreasing spacing between the boundaries toward northeast, as the narrow channel between Haltenbanken and the coast is approached. This is expected

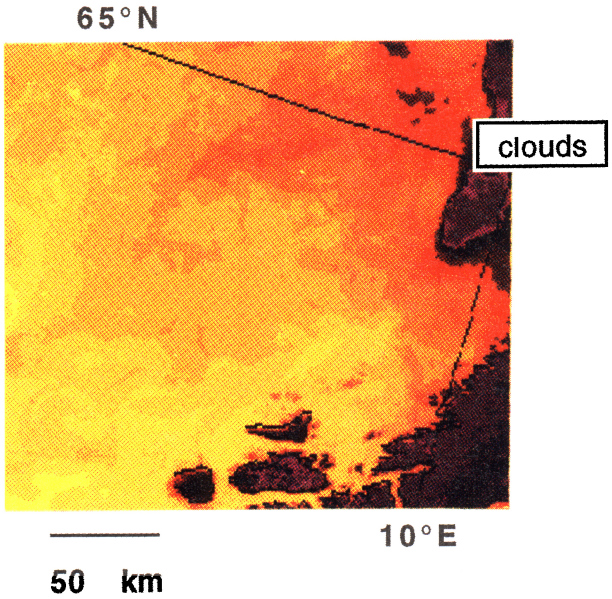

Plate 1. National Oceanic and Atmospheric Administration (NOAA) advanced very high resolution radiometer (AVHRR) satellite image of the sea surface temperature field obtained prior to the field campaign on October 29, 1991. The image covers the coastal region, including the SAR track shown in Figure 1b. Yellow indicates 9.5° to 10°C, decreasing stepwise in 0.5°C bands, to red, which is 7.5° to 8.0°C. Coastal islands and mainland are seen at bottom left.

owing to topographic steering of the coastal current [*Haugan et al.*, 1991]. There is also a tendency to find a concentration of the fronts along the coastal shelf break. In a few places, single fronts seem to split into several meandering fronts. Evidence of multiple frontal structures, in particular, connected with the zones of divergence and convergence, were also observed in the horizontal current vector and density variations (Figure 3 and Plate 2). The individual SAR image expressions are shown in Figures 4b–4f. The fronts meander across the images from near range to far range, appearing bright (maximum +3 dB relative to the background) some places and dark (maximum −2 dB relative to the background) other places. The frontal width varies from about 100 m to a few kilometres, and occasionally, the fronts are also characterized by a bright side followed by a dark side.

We interpret the expressions in Figures 4b–4f to be the manifestation of (1) converging and diverging frontal features within the NCC and (2) the NCC cyclonic shear boundary with the offshore water of Atlantic origin. These current patterns were both documented to exist by the ship measurements, although the ship transects did not exactly coincide in time with the SAR observations. As the short surface waves propagate into and/or across the current front, the amplitude and propagation direction changes. Since the wind speeds were moderate during these satellite overpasses, these changes in the short waves are detected by the SAR. Expressions of frontal features in SAR images are thus likely to reflect evidence of ageostrophic motion. During all 17 passes the sea surface temperature field was characterized by weak (1°C) thermal fronts. We thereby rule out any impact from thermal fronts on the variations in the radar cross section as discussed by *Askari et al.* [1993]. Evidence of similar ERS 1 SAR image expressions induced by short wave–current shear interaction are reported by *Liu et al.* [1994a] in the Gulf of Alaska, *Tilley and Beal* [1993] in the Gulf Stream, *Font et al.* [1993] in the western Mediterranean, and *Nilsson et al.* [1993] and *Nilsson and Tildesley* [1995] in the East Australian Current. In shallow water (50 m or less), moreover, spatial variations of the short wave–surface current interaction, induced by presence of topographic features like large sand waves and banks, are reported to be observed in ERS 1 SAR images under favorable conditions [*Vogelzang et al.*, 1994].

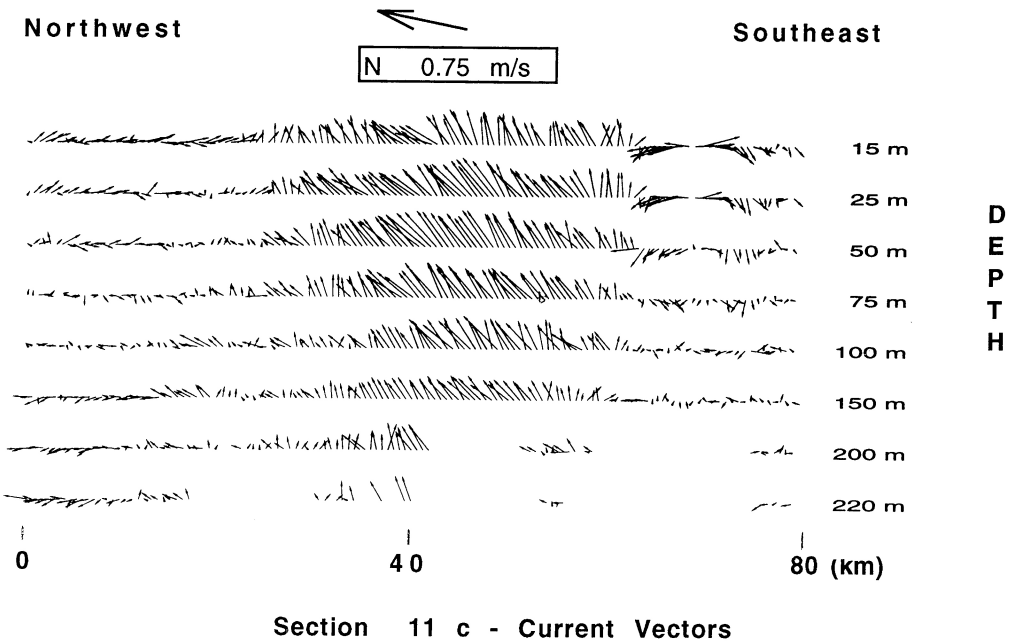

Figure 3. Current variability at selected depths between 15 and 220 m.

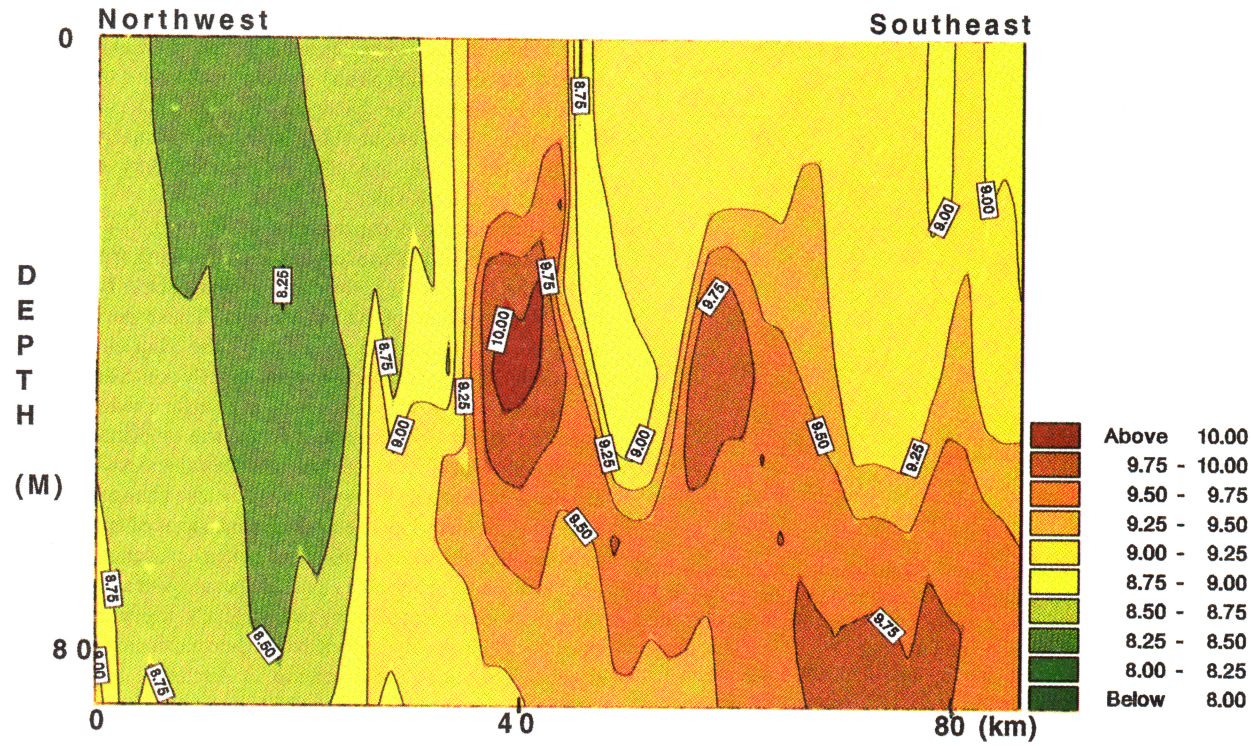

Section 11 c - Temperature

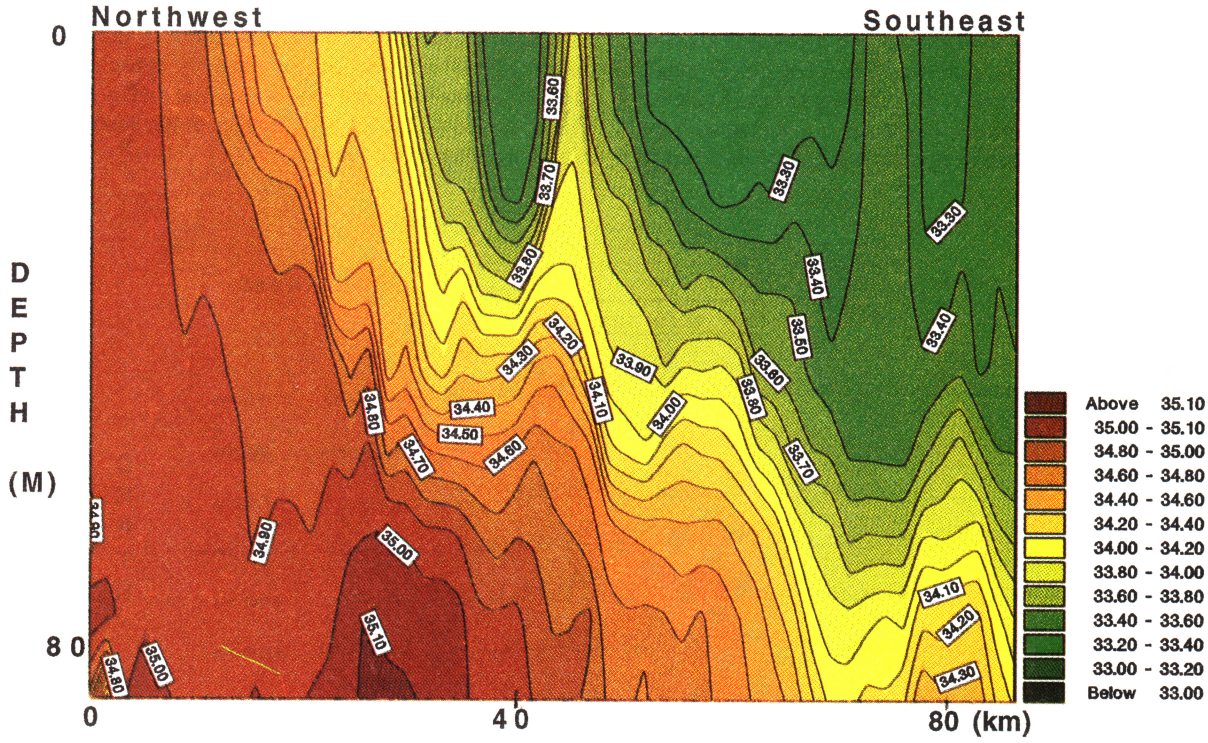

Section 11 c - Salinity

Plate 2. Vertical plots of (a) temperature, (b) salinity, and (c) density variations obtained on November 11 along the middle, near north-south section shown in Figure 2b.

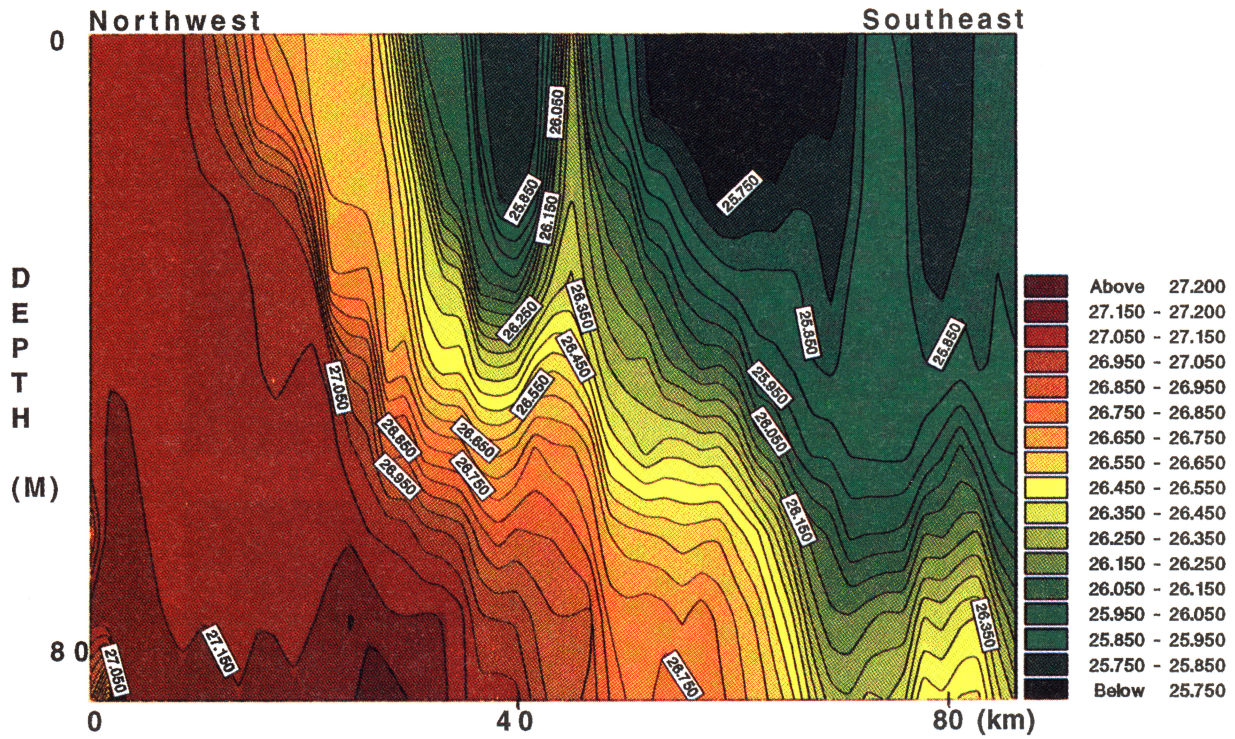

Plate 2. (continued).

2.2. The NORCSEX Follow-On Study

ERS 1 SAR images obtained along the west coast of Norway since launch repeatedly show meandering boundaries and mesoscale features in the NCC. Among these features the expression of eddies is usually the simplest to interpret.

2.2.1. SAR image expressions of eddies. Eddies can be manifested in SAR images through the short wave–current interaction outlining the curved shape of the eddy [*Johannessen et al.*, 1991] or as a series of curved boundaries characterized by concentric curvilinear lines of bright (dark) radar cross section [*Vesecky and Stewart*, 1982; *Liu and Peng*, 1993]. Alternatively, eddies can also be expressed indirectly through the presence of natural film trapped within spiraling lines associated with the eddy orbital motion [*Johannessen et al.*, 1993b]. In connection with eddies having strong thermal signals such as the warm or cold rings, the eddy can also be expressed through the wind stress change across the temperature front [*Lichy et al.*, 1981]. Along the coast of Norway the latter type of expression is rare.

In Figure 5a the SAR image obtained off the west coast of Norway on May 6, 1993, shows a cyclonic eddy with a diameter of 20 km through the spiral-shaped lines with very low radar cross section. We hypothesize that these lines are associated with small-scale turbulence aligned in the direction of the larger-scale eddy orbital motion. The turbulence, in turn, can lead to convective motion in the water that can bring organic material present in the upper layer to the surface, where it can remain as a microlayer of natural surface film [*Vesecky et al.*, 1986]. As the concentration of this surface film (surfactant molecules) increases, it can attenuate capillary and short gravity waves. In addition, the film edge may reflect the short waves that propagate at oblique angles to the edge, thus limiting the advance of the short waves through the slick, covered region. In turn, the lack of small-scale surface roughness reduces the radar backscatter, causing dark features or surface slicks. A closer examination of the image also suggests that the cyclonic eddy is part of a vortex pair, with the counterrotating anticyclonic eddy to the southeast.

The damping is strongly dependent on wind speed as well as film concentration. The expressions of the natural film typically disappear at higher winds (7 m s^{-1}), since wind-induced mixing in the upper layer will redistribute the surface slicks and prevent such damping [*Scott*, 1986]. In addition, the threshold wind speed value for the C band waves is estimated by *Donelan and Pierson* [1987] to be about 3.25 m s^{-1} at 10 m height above the surface. Hence, in order to contrast natural film, the fully developed 0.07- to 0.08-m waves necessary to provide resonant Bragg backscatter are needed. When such waves are present, slicks can lead to a backscatter contrast of about 6–10 dB. During SAR acquisition the average wind was about 5 m s^{-1} from northwest as reported in the analyzed weather map. We therefore assume that the backscatter front and larger region of low radar return as seen in the eastern sector are expressed by the wind dropping below threshold.

The appearance of slicks associated with mesoscale and submesoscale eddies in spring and summer is perhaps an indirect indication of the spring and summer bloom in the upper layer along coastal zones. Apart from the standard weather observations along the coast, no surface data are available to offer sufficient analysis of the physical and biochemical conditions in the cyclonic eddy or vortex pair. *Gower* [1993] and *Nilsson and Tildesley* [1995] report similar findings, along the west coast of Canada and East Australian Current, respectively. After the launch of Seastar in the spring of 1995, near-coincident sea-

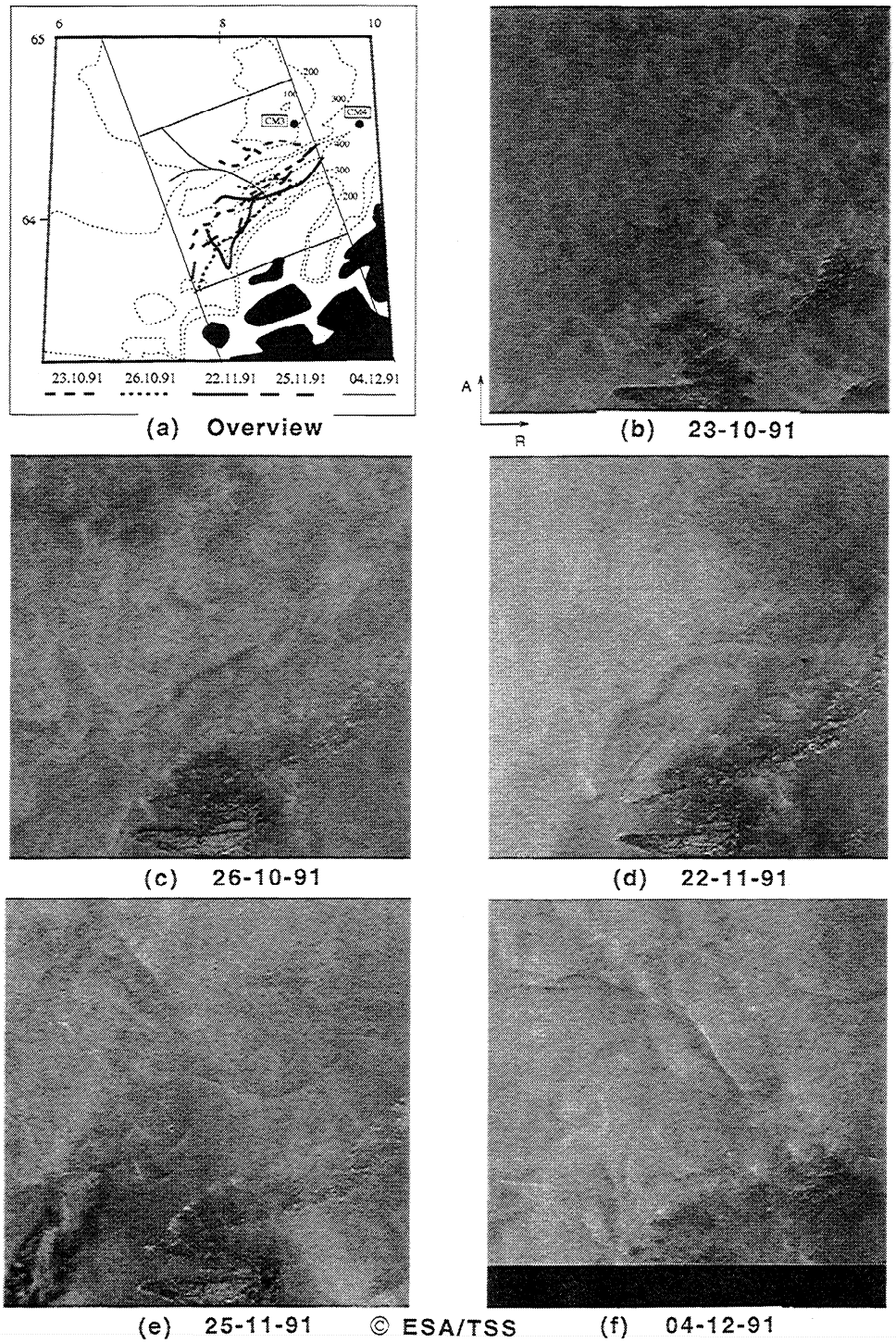

Figure 4. (a) Collection of frontal boundaries found in the five ascending SAR images from October 23 until December 4, 1991. Isobaths and positions of CM3 and CM4 are also shown. The five corresponding 100-m resolution ERS 1 SAR images (100 km × 100 km) showing both bright and dark fronts for (b) October 23, with range and azimuth marked at bottom left; (c) October 26; (d) November 22; (e) November 25; and (f) December 4. The maximum and minimum radar backscatter (in decibels) for the central regions covering the frontal boundaries (paired for each of the images, according to the dates) are −2.7, −6.7; −3.0, −8.9; −2.0, −7.4; −2.5, −7.0; and −2.8, −8.3, respectively.

viewing wide field-of-view sensor (SeaWiFS) and SAR images can be examined to see if any correlation exist between presence of surface film, ocean color, and mesoscale circulation pattern.

In contrast to the eddy expressed through the presence of natural slicks, the SAR image obtained on December 2, 1993, depicts a cyclonic eddy feature through short wave–current interaction (Figure 5b). The eddy diameter is about 10 km, and

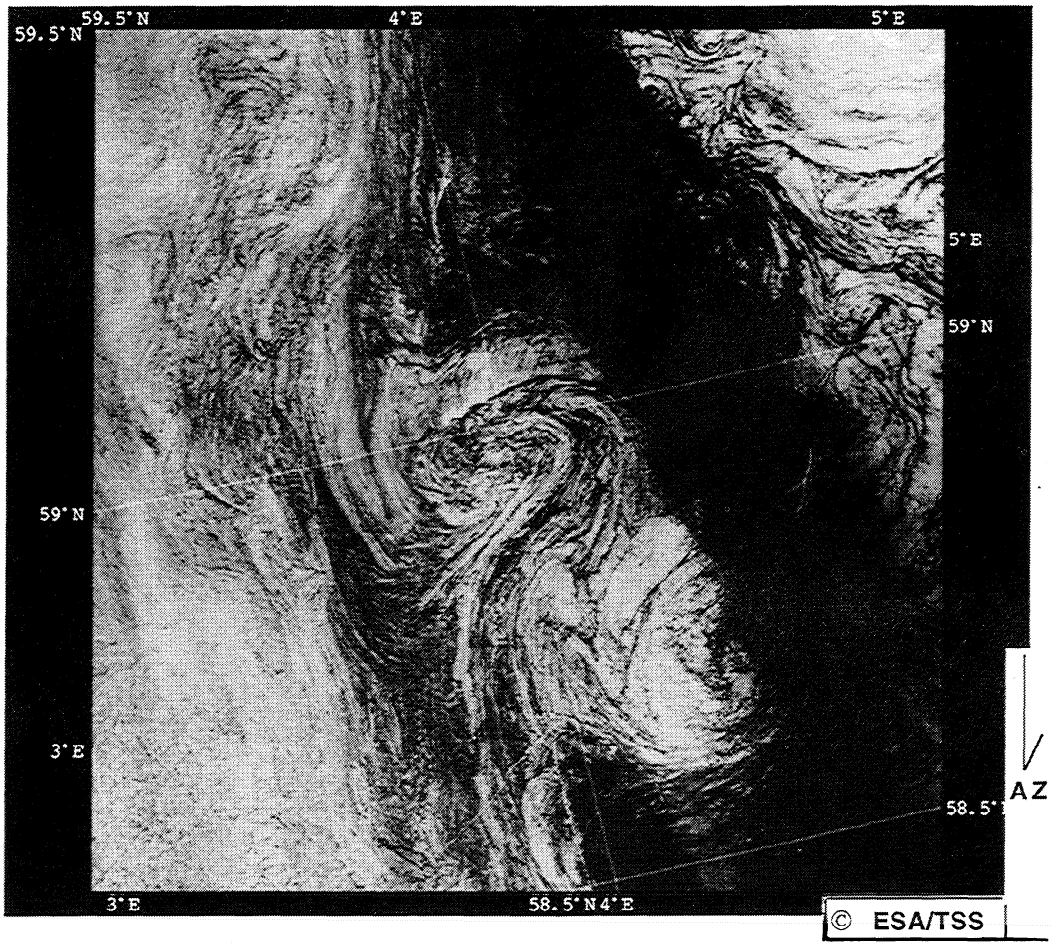

Figure 5a. ERS 1 SAR image (100 km × 100 km) obtained off the west coast of Norway on May 6, 1993, expressing a 20- to 30-km in diameter cyclonic eddy feature through spiraling lines assumed to be natural film at sufficient concentration to dampen out the Bragg waves. Maximum and minimum radar backscatter (in decibels) range from −9.5 to −25.5.

it is located at the crest of an elongated frontal boundary further discussed in the next section. In this case the varying radar cross section along the eddy boundary apparently is due to variations in the look direction relative to the eddy boundary (as discussed further in section 3) as well as possibly spatial variations in the current pattern along the eddy boundary.

These synoptic manifestations of the eddy rotational direction, horizontal dimension, and spiraling lines suggesting surface convergence are clearly important for studies of mesoscale coastal circulation and water quality. Moreover, they offer a valuable opportunity for comparison and validation of simulations of surface current pattern, despite the lack of complete understanding of the imaging mechanisms [*Johannessen et al.*, 1993b, c].

2.2.2. SAR image expressions of current fronts. An excellent documentation that the frontal features associated with the mesoscale circulation patterns are expressed in SAR images is shown in Plate 3, where the radar-derived surface roughness patterns are compared with the NOAA IR-derived sea surface temperature [*Johannessen et al.*, 1995]. The NOAA AVHRR image (Plate 3, left) and the ERS 1 SAR image (Plate 3, right) were obtained about 7 hours apart on October 3, 1992, off the west coast of Norway. In the IR image the surface temperature decreases from nearly 14°C (white) in the coastal water to 12°C (purple) in the Atlantic water offshore. The sea surface temperature of 13.5°C reported from the Seawatch Europe buoy (location marked by plus in Plate 3, left) was used to retrieve the absolute surface temperature based on the assumption of a linear relationship between the sea surface temperature and the image brightness temperature. The fairly weak temperature contrast is typical of this time of the year. The maximum temperature gradient is about 0.6°C km^{-1}. Previous observations across such temperature fronts have established corresponding salinity and density fronts, which combine to maintain a baroclinic current boundary. The structure of the sea surface temperature field with the curvilinear temperature fronts represents mesoscale variability of 10 to 50 km scale, characteristic of the unstable Norwegian Coastal Current [*Johannessen et al.*, 1989].

The ERS 1 SAR image (Plate 3, right), acquired 7 hours later, contains frontal features at a scale, configuration, and orientation that are in good qualitative agreement with those seen in the IR image. The SAR image shows both bright and dark radar cross-section modulations of various width across the boundaries. It clearly verifies that the SAR can image current boundaries, including meanders. On the basis of the surface weather analysis, the winds were northerly at 5 m s^{-1}, with air temperatures from 12° to 14°C reported along the coast where the images were acquired. Furthermore, a northward near-surface current of 0.30 m s^{-1}, a constant tempera-

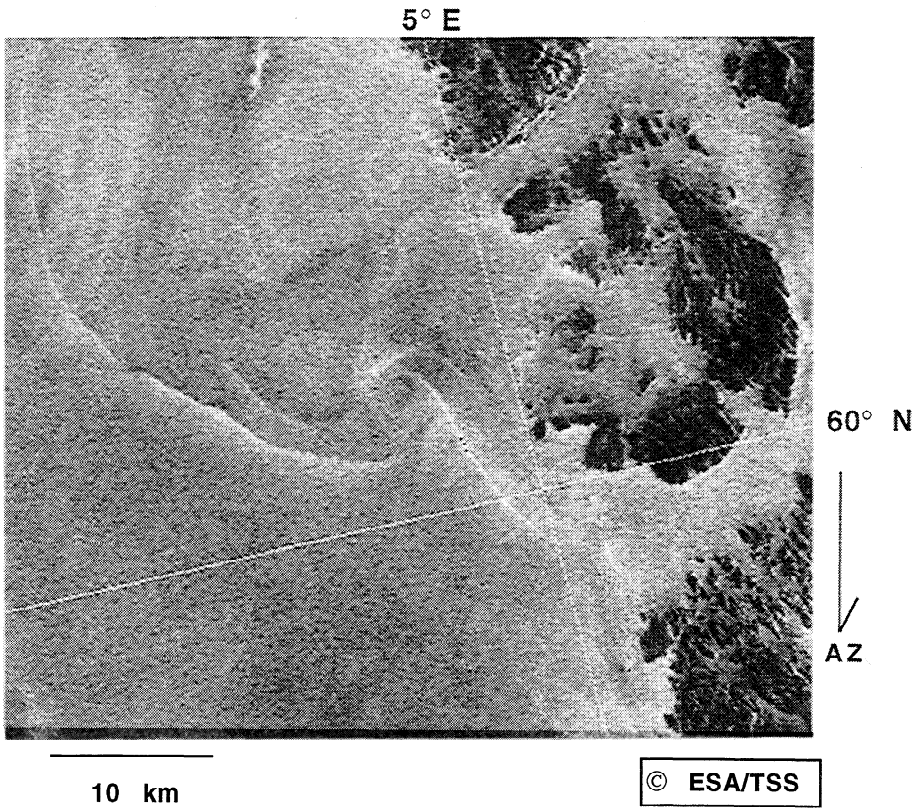

Figure 5b. SAR image obtained off the west coast of Norway on December 2, 1993, showing a 10-km in diameter cyclonic eddy depicted through short wave–current interaction. The image size is about 50 km × 40 km. Maximum and minimum radar backscatter (in decibels) range from −4.0 to −11.0.

ture of about 13.5°C in the upper 20 m of the water column, and a significant wave height of 1 m were reported at the ERS 1 satellite overpass time from the moored Seawatch buoy (Plate 3, left).

The air-sea temperature difference indicates near-neutral stability. We might thus expect that backscatter variations could be modulated by the wind stress variations induced by the changes in boundary layer stratification [*Brown*, 1990] in the vicinity of the frontal boundary. An increase in the surface wind stress due to a drop in the stratification will cause an increase in the surface roughness and, in turn, in the radar cross section. This is examined in Figure 6 (top) by relating the observed radar cross section to the wind speed using CMOD4 (the ERS 1 scatterometer wind retrieval model) which assumes neutral stratification [*Stoffelen and Andersen*, 1993]. A mean wind speed of about 6.2 m s^{-1} is obtained, in good agreement with the weather reports. By subtracting this mean wind speed and corresponding radar cross section, we can relate the remaining radar cross-section fluctuations to the atmospheric stratification [*Wu*, 1991] as shown in Figure 6 (bottom). Assuming constant air temperature, we consider the sea surface temperature variations to represent the fluctuations in the stratification. The results suggests that the bright (1-dB increase), narrow peak at 25 km ground range would require almost −6°C unstable stratification to be totally attributed to a wind stress change. Moreover, the second bright peak at 80 km ground range would require about −12°C unstable stratification. Although we lack detailed spatial and temporal information of the air temperature and the wind speed, this appears to be too much, according to the weather analyses. We therefore conclude that the SAR image expressions primarily reflect the wave-current interaction for the short gravity waves along the current fronts. As the short gravity waves, i.e., from centimeter waves to meter waves, propagate across the current front, they change steepness and propagation direction. The combined effect, in turn, leads to the increase in the radar cross section.

In an attempt to better quantify the correlation between the features seen in the two images, we enhanced the feature edges as shown in Figure 7 using a "Marr wavelet" [*Marr and Hildreth*, 1980; *Farge*, 1992]. The Marr wavelet amounts to a band-pass filter with a selectable scale setting (or smoothing). In this case the scale was set at 1 km for each image. The zero crossings of these images identify edge locations and orientation at the selected scale. It clearly confirms that the wavelet method is well suited for automatic edge detections in SAR images as suggested by *Liu et al.* [1994, b]. The cross-correlation coefficient between the two images indicates the level of agreement. In this case, maximum cross correlation between the edge-enhanced SAR and AVHRR image was about 70% for subscenes of 18 km by 18 km, indicating that the same basic oceanic process or feature is being sensed in both images. A larger subimage results in a lower cross-correlation value. This is indicative of the shifts in the relative position and scale of the various features due to the temporal difference between the two images and the fundamentally different ways in which the two images are formed.

Another documentation that the SAR is capable of detecting frontal boundaries is shown in Figure 8. This image was obtained from the descending pass on December 2, 1993. During the 3-hour period centered at image acquisition, coastal

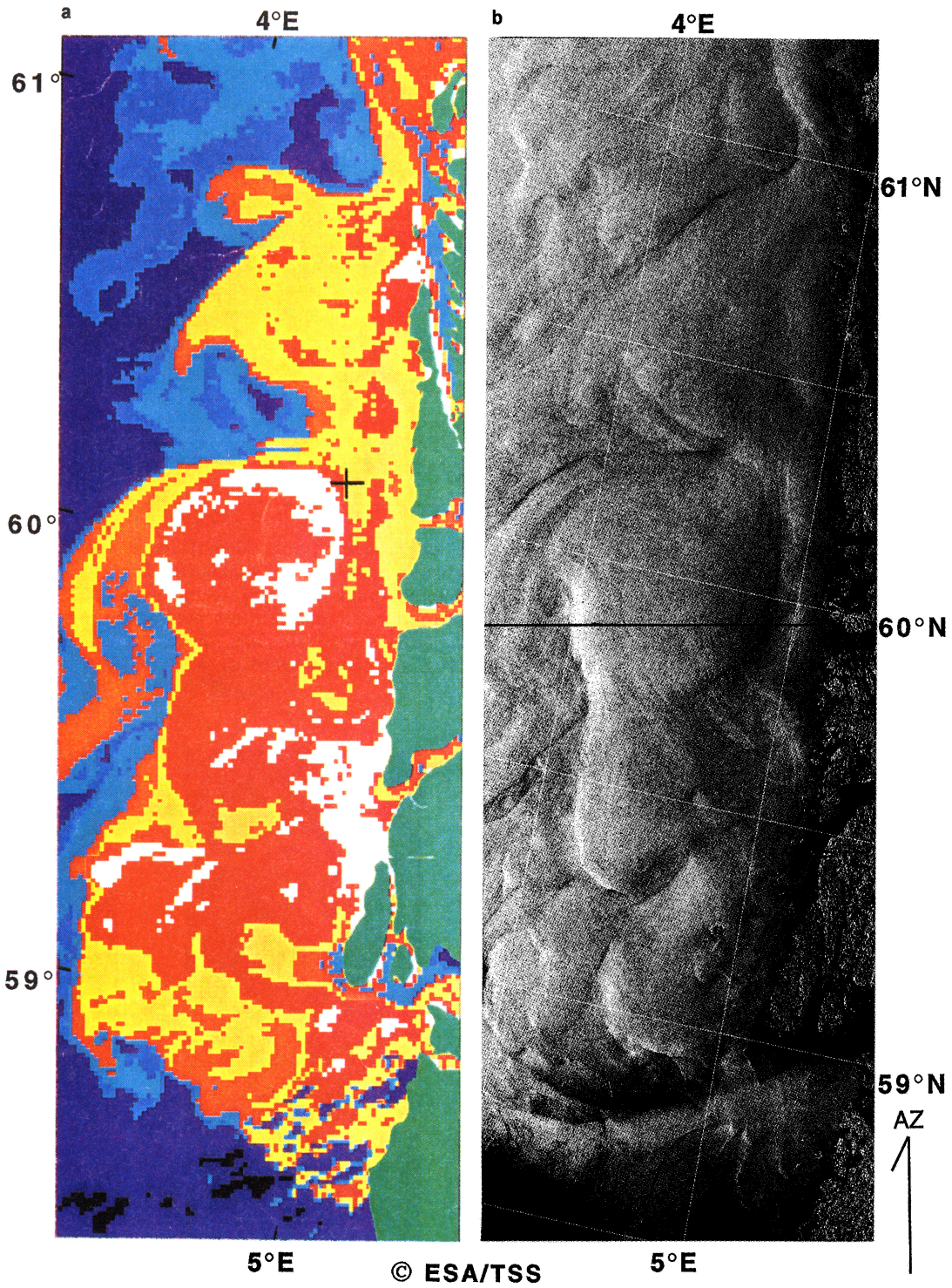

Plate 3. Comparison of a (left) 1-km resolution NOAA 11 AVHRR IR image acquired at 1420 UTC on October 3, 1992 (white is 14°C and purple is 12°C; plus denotes buoy position; and land is masked in green and clouds in black) and (b) 100-m resolution ERS 1 SAR image acquired at 2135 UTC on October 3, 1992. Both images cover the same 100 km by 300 km region off the west coast of Norway between 59° and 62°N.

meteorological stations reported increasing southwesterly winds from about 5 to 10 m s^{-1}. Again, the meandering structure of the NCC is expressed, in this case mostly as bright changes in radar cross section, at wavelengths of 10 to 50 km. In several places the pattern is characterized by parallel fronts, and as for the SAR image discussed in Plate 3 (right), the mean distance from the front to the coast decreases with increasing latitude. This was also observed by *Johannessen et al.* [1989], who argue that the topographically steered recirculation of the Atlantic Water in the Norwegian Trench was most effective north of 60°30′N.

These results suggest that in spaceborne monitoring of me-

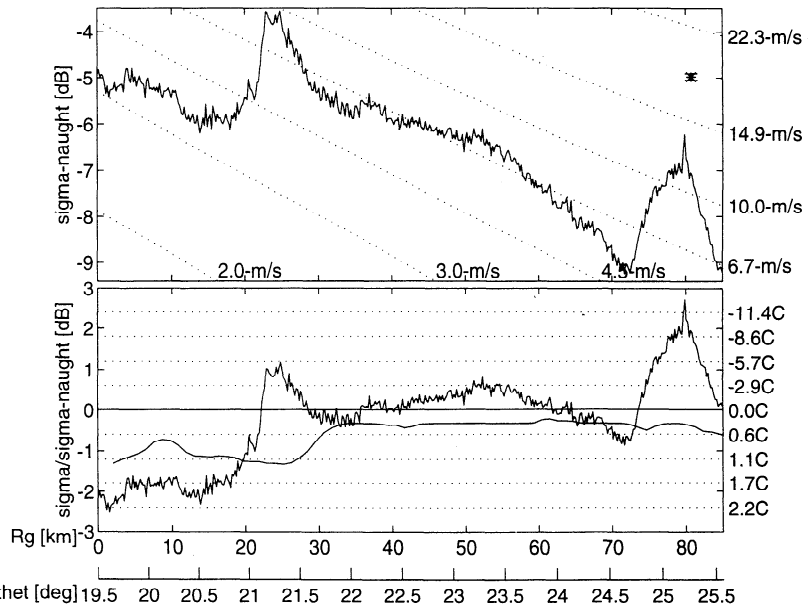

Figure 6. (top) Profile of radar cross section (in decibels) (extracted from the SAR image in Plate 3 (right), along the inserted line) versus wind speed using coordinates based upon CMOD4 (the ERS 1 scatterometer wind retrieval model). The dotted lines represent different wind speeds by assuming that the radar look direction is cross wind. The error bar for the cross-section measurements is indicated at top right. (bottom) Changes in relative cross section interpreted in terms of atmospheric stability. The sea surface temperature profile taken from the AVHRR is shown relative to 14°C (or neutral stratification).

soscale coastal ocean circulation, the SAR-derived current boundaries can replace the IR-derived sea surface temperature fronts in the event of total cloud cover. Under conditions with partial cloud cover the SAR can be used to connect the sea surface temperature fronts masked by the clouds. In general, the local wind speed will restrict the ability of SAR to detect surface-current-related features. Winds between 3 and 10 m s^{-1} are favorable for surface current feature detection by SAR [*Johannessen et al.*, 1995]. Therefore combined use of near-coincident SAR and IR images both improves and optimizes the spaceborne observations of mesoscale ocean circulation features. Moreover, this enables the remote sensing data to become more attractive for assimilation in monitoring and modeling of the marine coastal environment [*Johannessen et al.*, 1993c].

3. SAR Image Simulations

In order to quantify geophysical parameters from SAR imagery, it is first necessary to understand how the parameters affect the radar cross section and to determine, in particular, whether any unique relationship exists between the image expressions and the dominant geophysical parameters. The next stage is then to invert the process, i.e., to go from the radar cross-section perturbations back to the underlying geophysical processes. SAR simulation models based on the two-scale backscatter model coupled with the wave action equation (to determine how the wave spectrum is modified by interaction with the current) have had some success in modeling, at least qualitatively, the observed SAR radar cross-section features, although they tend to underpredict the absolute value of the perturbations, particularly at X and C bands [e.g., *Lyzenga*, 1991]. The inverse problem of estimating the underlying geophysical processes that caused the SAR image feature has not

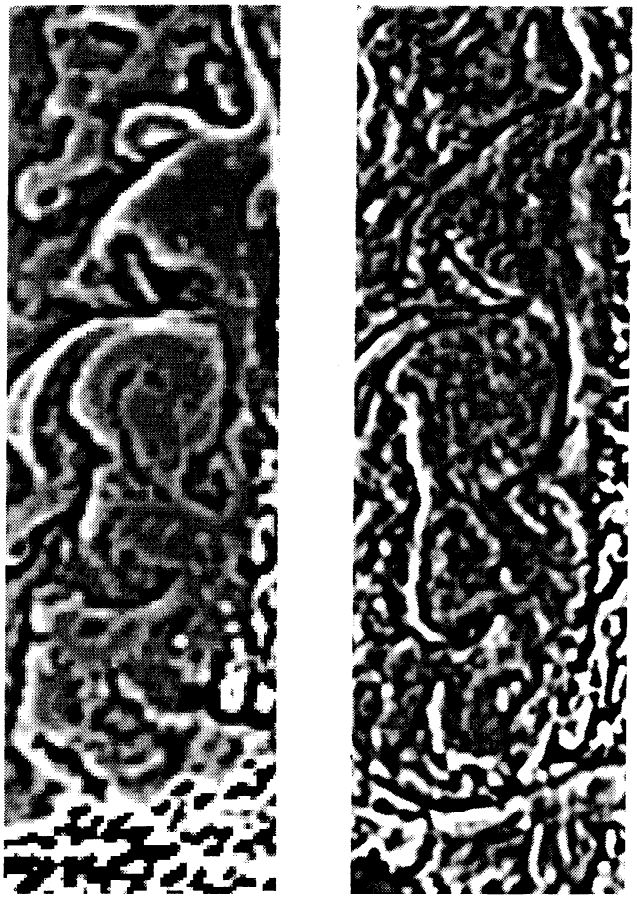

Figure 7. Edge enhancement of the (left) IR image and (right) SAR image shown in Plate 3 using a Marr wavelet [*Marr and Hildreth*, 1980] (see text).

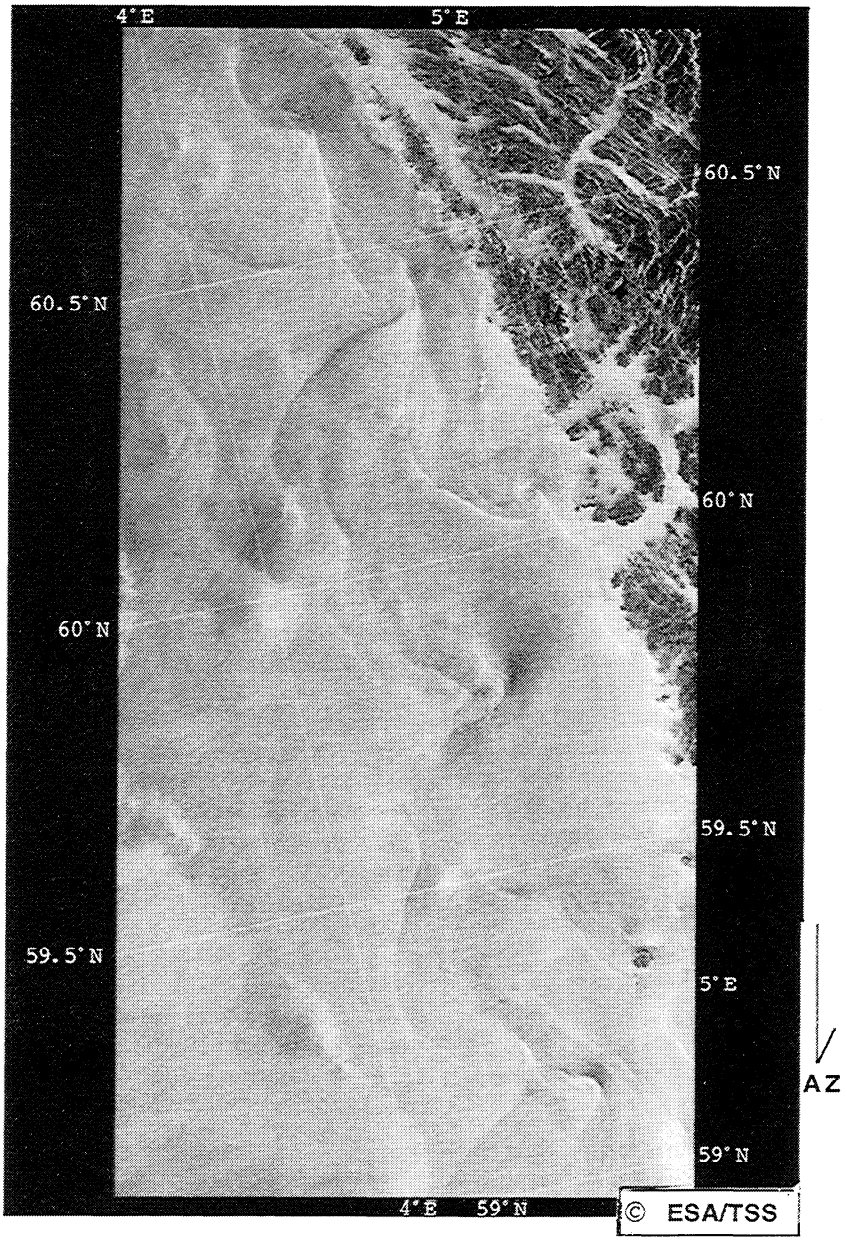

Figure 8. SAR image of the frontal boundary of the Norwegian Coastal Current obtained on December 2, 1993. Maximum and minimum radar backscatter (in decibels) range from −4 to −12.2. A subscene of this image is shown in Figure 5b.

been as intensively investigated to date, and relatively few examples of such inversion have been reported in the literature.

In SAR images of a curving current front (Plate 3) it is often observed that the radar cross-section perturbation across the front can change sign, i.e., go from a bright to a dark perturbation, as a function of position along the front. In the previous section we interpreted these expressions, in general, to reflect short wave–current interaction, in particular, from strong current shear and zones of surface convergence and divergence, without further consideration of the frontal dynamics. Here we will apply an SAR simulation model to determine which combinations of shear (dv/dx) and convergence ($du/dx < 0$) or divergence ($du/dx > 0$) produce bright and dark image features. Thus, by simply observing the contrast and orientation of linear features in the image, we can place some constraints on the frontal characteristics. By making additional assumptions, for example, that the characteristics of the front remain constant while the orientation of the front changes or that the magnitude of the shear is much larger then that of the strain, additional inferences can be drawn from the images. This method uses only relative changes in radar cross section; the absolute values of the perturbations are not required.

The SAR simulation model we shall use was developed by *Lyzenga* [1991], and we will follow the coordinate system defined there. We assume that locally (on scales of several hundred meters), the front can be considered to be linear or one-dimensional. Thus we define a local coordinate system such that the x axis is orthogonal to the front and the y axis is parallel to the front at a given location. Moreover, we assume

that within this coordinate system the current changes only in the x direction and is constant in the y direction, although the current may have components in both directions as denoted by $u(x)$ and $v(x)$, respectively. Since the calculation is made locally, we do not need to assume that the currents are the same at all locations along the front, but only that any along-front variations are much smaller than the cross-front variations. In the following we will assume that the radar return is dominated by Bragg scattering, so we will be interested in the changes in the amplitude or spectral density of the Bragg wave (which has a wavenumber of $k_B = 2k_0 \sin(\theta)$, where k_0 is the radar wavenumber and θ is the incidence angle) as it propagates across the front at a propagation direction of either ϕ or $\phi + 180°$, where ϕ is the radar look direction relative to the x axis. For the smaller ERS 1 incidence angles (near 20°), specular scattering may also contribute to the radar backscatter, and at all angles the Bragg backscatter may be modified by surface tilt effects due to longer surface waves. Inclusion of these effects (especially the second one) would modify the conclusions presented below to some extent because they introduce scattering mechanisms involving waves that are longer than the Bragg wavelength and are not traveling exactly in the line of sight direction. However, it can be assumed that waves traveling in the line of sight direction still dominate the backscatter, even if these mechanisms are included, and under this assumption our conclusions will remain valid. It may be noted, moreover, that the wavelength does not explicitly enter the following derivation, although it is assumed that the wavelengths influencing the backscatter are short enough so that their relaxation rates β_r are large enough compared to $(c_{gx} + u)/L$, where c_{gx} is the component of their group velocity in the x direction and L is the characteristic length of the current pattern.

If we let the surface wave height equilibrium spectrum $S_0(k, \phi)$ be modeled as

$$S_0(k, \phi) = c_n k^{-p} \cos^{2n}\left(\frac{\phi - \phi_W}{2}\right) \tag{2}$$

where p and n are parameters that control the spectrum falloff in k and ϕ, respectively, and ϕ_w is the wind direction, then we can write the spectral perturbation $f(k, \phi)$ caused by propagating through the current front as

$$f(k, \phi) = \frac{\left[\cos(\phi)\frac{du}{dx} + \sin(\phi)\frac{dv}{dx}\right]}{\beta_r} \cdot \left[-\left(p + 1 - \frac{c_g}{c}\right)\cos(\phi) + n\sin(\phi)\tan\left(\frac{\phi - \phi_W}{2}\right)\right] \tag{3}$$

where c is the surface wave phase speed.

Using σ_0 to denote the equilibrium or background radar cross section per unit area and σ_f to denote the radar cross section perturbed by the frontal currents, then the relative radar cross-section change across the front can be written as

$$\frac{\sigma_f - \sigma_0}{\sigma_0} = \frac{S_0(k, \phi) f(k, \phi) + S_0(k, \phi + \pi) f(k, \phi + \pi)}{S_0(k, \phi) + S(k, \phi + \pi)} \tag{4}$$

where we have taken into account the Bragg waves propagating both toward and away from the SAR. By substituting (2) and (3) into (4) and performing some algebra, we get

$$\frac{\sigma_f - \sigma_0}{\sigma_0} = \left(\frac{\sqrt{(du/dx)^2 + (dv/dx)^2}}{\beta_r}\right)\cos(\phi - \psi)\, g(\phi, \phi_W) \tag{5}$$

where

$$g(\phi, \phi_W) = \left\{-\left[p + 1 - \frac{c_g}{c}\right]\cos(\phi) + n\sin(\phi) W\left[\frac{\phi - \phi_W}{2}\right]\right\} \tag{6}$$

$$\psi = \tan^{-1}\left(\frac{dv/dx}{du/dx}\right) \tag{7}$$

$$W(\phi') = \frac{\cos^{2n-1}(\phi')\sin(\phi') - \sin^{2n-1}(\phi')\cos(\phi')}{\cos^{2n}(\phi') + \sin^{2n}(\phi')} \tag{8}$$

The parameter Ψ indicates the relative strength of the shear (dv/dx) versus convergence (du/dx) across the front.

We can now utilize (5) to determine the ranges of relative SAR look angles ϕ for which the radar cross-section perturbation should be bright or dark. We are particularly interested in the values of ϕ for which (5) equals zero, since these will be the angles for which the sign of the radar cross-section perturbation changes. Note that the first factor in (5) simply scales the perturbation by the strength of the currents and the relaxation rate. Since we have already incorporated the Bragg waves propagating both toward and away from the SAR, we only need search over values of ϕ in the interval $-90, 90°$. Note that as the current front curves through the SAR image, the relative SAR look angle ϕ will change (since it is defined with respect to the front direction) but the difference between the relative SAR look angle and the relative wind direction $(\phi - \phi_W)$ will remain constant. This implies that the term $W[(\phi - \phi_W)/2]$ in (6) will be a constant for any given SAR image.

To determine when (5) equals zero, we first examine $g(\phi, \phi_W)$. This term will be zero when

$$\tan(\phi) = \frac{\left(p + 1 - \frac{c}{c_g}\right)}{nW\left(\frac{\phi - \phi_W}{2}\right)}. \tag{9}$$

For the Bragg wavenumber corresponding to the ERS 1 SAR parameters, c_g/c is approximately 0.5. Using values of p in the range of 4 to 7 and letting $n = 2$, (9) implies that $g(\phi, \phi_W)$ is always negative for $-80° < \phi < 80°$. For this range of look angles (which encompasses most cases of interest) the sign of the radar cross-section perturbation is therefore opposite to the sign of $\cos(\phi - \psi)$.

A simple geometric representation of this relationship is possible by considering a plot of du/dx versus $-dv/dx$ as shown in Figure 9. Such a plot is convenient for representing the expected radar cross-section perturbations induced by surface current fronts. For example, points on the left side of this plot correspond to converging (downwelling) fronts, points on the right correspond to diverging (upwelling) fronts, points on the upper half correspond to anticyclonic shear, and points on the lower half correspond to cyclonic shear. Most of the fronts encountered in the NCC are dominated by cyclonic shears with alternating weak convergence and divergence and would be represented by points near the lower half of the vertical axis.

If a line is drawn through the origin of this plot in Figure 9, having the same orientation as that of a front in the SAR image (assuming the image is oriented with the SAR look direction either to the right or to the left as in Plate 3), then fronts represented by points to the left of this line will be imaged as bright lines and points to the right will be imaged as dark lines.

In Plate 3 most of the linear features that are oriented such that $\phi < 0$ (i.e., running from lower right to upper left) are bright, while most of those with $\phi > 0$ (i.e., running from lower left to upper right) appear as dark lines. Referring to Figure 9 and assuming we have prior knowledge that $|du/dx| < |dv/dx|$; that is, the fronts are shear dominated, we can infer that $dv/dx > 0$; that is, the shear is cyclonic.

On the other hand, there are some vertically oriented features (with $\phi = 0$) which appear as bright lines and some which appear as dark lines (Plate 3). Since the shear has no effect for these cases, those features which appear as bright lines must be associated with converging currents and those which appear as dark lines must indicate diverging currents, assuming, of course, that only wave-current interactions are involved in the formation of the features. This is consistent with SAR observations of range-traveling internal waves. The convergence zones, we believe, may be interpreted as regions within a meandering front which are advancing offshore, while the divergence zones correspond to regions of such a front which are receding shoreward.

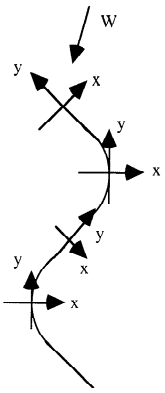

position	relative wind direction	relative look direction
a	210	-45
b	255	0
c	300	45
d	255	0

Figure 10. Simplified two-dimensional representation of a meandering front with crest in position d and the trough in position b. The wind direction is marked W. The local coordinate system, along with corresponding relative wind direction and relative look direction measured counterclockwise from the x axis, is listed for four positions along the front. The magnitudes of current shear and convergence/divergence are listed in Table 1.

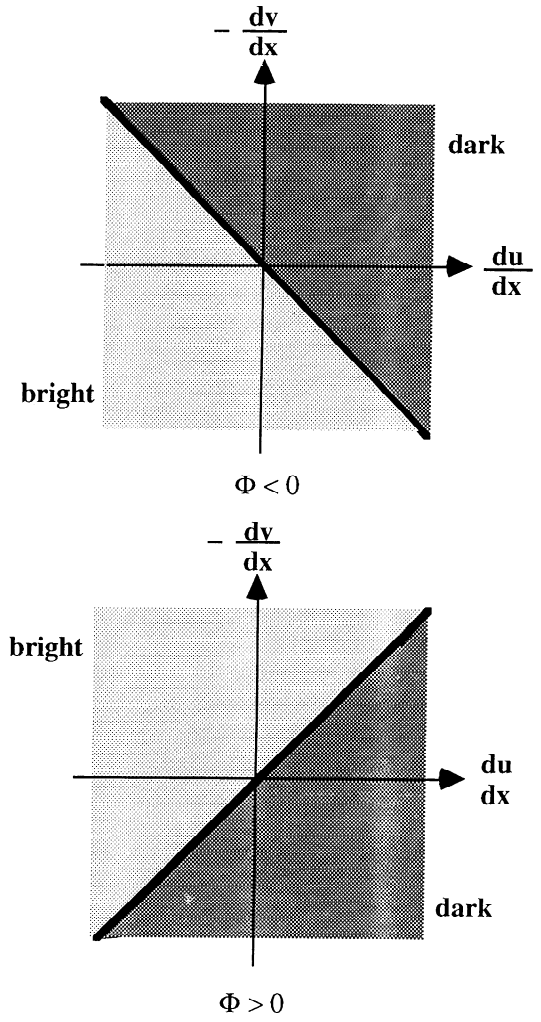

Figure 9. Ranges of du/dx and dv/dx resulting in bright and dark perturbations for a given front orientation. The orientation of boundaries in these plots corresponds to the orientation of fronts in the image, assuming radar look direction is either to the right or to the left.

In Figure 10 we show a simplified two-dimensional representation of such a meandering front, along with the corresponding wind direction and look direction measured counterclockwise from the x axis. The front has a constant cyclonic current shear of $5 \times 10^{-3}\ s^{-1}$, along with four combinations of convergence and divergence which we have labeled as cases 1 through 4 in Table 1. The resulting radar cross-section values at four locations along the front are also given in Table 1. For all cases the perturbation is positive (bright) at position a and negative (dark) at position c. However, the sign of the perturbation at the "trough" of the meander (position b) changes from negative to positive, depending on the value of the convergence or divergence at this location. At the "crest" (location d) the perturbation is either positive or zero for all cases considered. From the patterns observed in Plate 3, we conclude that case 1 is the most likely existing condition, as it provides the same qualitative trend in radar backscatter perturbation. The existence of regions of convergence (downwelling) and divergence (upwelling) at the crest and trough may reflect the state of the meander, i.e., whether the meander is growing or decaying. Moreover, such conditions may, in turn, have significance for the biological activities along the front.

The magnitude of the predicted perturbation, on the other hand, depends strongly on the angular dependence of both the equilibrium spectrum and the relaxation rate. Since these are uncertain, it is difficult to draw definitive conclusions regarding the quantitative accuracy of the model, and quantitative comparisons would therefore not necessarily be meaningful. In general, our model predictions tend to underestimate the contrast observed in the images, but we are uncertain as to whether this is due to inadequacies in the model or whether the current gradients inferred from our in situ measurements and used in our model calculations are smaller than the actual current gradients occurring near the surface.

Table 1. Intercomparison of Radar Cross-Section Perturbations Predicted by the Synthetic Aperture Radar Simulation Model for the Meandering Current Front and Corresponding Changes in Local Wind and Look Directions Using Four Combinations of Shear Versus Convergence and/or Divergence

Relative Wind Direction, deg	Look Direction, deg	Current Shear dv/dx	Convergence or Divergence, s^{-1}				Radar Cross-Section Perturbation			
			Case				Case			
			1	2	3	4	1	2	3	4
210	−45	0.005	0	0	0.002	−0.002	0.206	0.206	0.136	0.264
255	0	0.005	0.002	0	0	−0.002	−0.142	0	0	0.158
300	45	0.005	0	0	−0.002	−0.002	−0.180	−0.180	−0.102	−0.102
255	0	0.005	−0.002	0	0	−0.002	0.158	0	0	0.158

See Figure 10.

4. Summary

From the number of SAR images examined from the coast of Norway and the use of an SAR image simulation model we have revealed the following.

1. Presence of natural film is frequently seen expressing spiraling eddies during the summer months, with damping in the radar cross section of up to 6–10 dB. Damping by the natural films appears possible up to about 7 m s^{-1} at C band, vertical polarization, suggesting that both the dominance of moderate winds and the increased biological productivity in summer appear favorable for ocean feature detections by the SAR through the presence of natural film. When synoptic SAR and SeaWiFS observations become available, this hypothesis may be further explored.

2. Meandering fronts are mostly expressed by the short wave–current interaction, leading to both bright and dark radar cross-section perturbations reaching up to +/−3 dB relative to the background mean. In situ current and thermohaline measurements obtained in between the SAR acquisitions suggest that the persistent strong current shear and the convergence/divergence are likely to cause this radar cross-section perturbations.

3. At C band, winds below 2 to 3 m s^{-1} may lead to areas of low radar return, since resonant Bragg waves of about 0.07–0.08 m wavelength are not fully developed. Above 10–12 m s^{-1}, expressions of the oceanic features vanish, since the spatial distribution of the short gravity waves is predominated by the wind stress field, the wind wave, and eventually, the swell field.

4. Under favorable image conditions the cross correlation between the surface roughness pattern imaged by SAR and the sea surface temperature distribution imaged by AVHRR is up to 70%. This high value indicates that the same basic oceanic process or feature is being imaged by both sensors, supporting the interpretation that the two images have the surface current boundaries in common. This furthermore suggest that in the spaceborne monitoring of mesoscale coastal ocean circulation, the SAR-derived current boundaries can replace or connect the IR-derived sea surface temperature fronts in the event of total or partial cloud cover. Consequently, combined use of near-coincident SAR and IR images both improves and optimizes the spaceborne observations of mesoscale ocean circulation features.

5. The SAR image simulation model suggests that the convergence and divergence along the front have significant impact on the radar cross-section perturbations. In particular, in regions where the front is orthogonal to the look direction, bright radar cross-section perturbations imply convergence and dark perturbations imply divergence. Therefore, in such cases the SAR images can be used to interpret frontal dynamics, including growth and decay of meanders, upwelling, and downwelling. However, in spite of the apparent qualitative agreement, the magnitude of the predicted perturbation is uncertain due to several factors, including lack of knowledge of the angular dependence of both the equilibrium spectrum and the relaxation rate.

Continuing systematic SAR image simulation studies is necessary to advance the consistency between the simulation models and SAR observations and to establish whether unique relationships exist between the image expressions and the dominating geophysical quantities. In particular, better model formulation must be provided, including parameterization of wave breaking, wave growth, nonlinear wave-wave interaction, and sensitivity of the directional distribution of the short wave action spectrum on the wind direction. Better quantitative wind field estimates from the SAR image will also provide better capabilities for obtaining quantitative interpretation of mesoscale ocean circulation features, since submesoscale wind field variations are easily captured in SAR images, especially at moderate to low winds. Moreover, it is important to better quantify the spatial distribution and gradients of the surface current field coincidently with the SAR overpass such as proposed in several studies under the second ERS announcement of opportunity.

Regular access to multisensor, high-resolution satellite data, integrated with in situ measurements and numerical models, is an important and necessary element in coastal ocean monitoring and prediction systems that include data assimilation [*Johannessen et al.*, 1993c]. The launch of SeaWiFS in 1996 together with ERS 2 and Radarsat within 1995 will provide opportunities for the combination of AVHRR and ERS 1 satellite data to obtain near-coincident observations of the sea surface temperature, the color, and the roughness at significantly improved temporal and spatial coverage. In particular, the wide swath (500 km) coverage obtained with Radarsat, together with ERS 1 and ERS 2 SAR provides improved capabilities to regularly monitor the temporal and spatial variabilities on 3–10 days and 10–100 km. Satellite SAR, independent of clouds, fog, and light conditions, may therefore play a vital role in the success of such an integrated system.

Acknowledgments. Core support for this study was provided by Norwegian Space Center (NSC) under the contract "Norwegian ERS-1 Application Project," the European Space Agency (ESA) under an SAR Feasibility Study contract, and the Oceanographer of the Navy/NRL-south, United States. Additional support was provided by Geophysical Institute, University of Bergen, Office of Naval Research, and NATO Collaborative Research Grants Programme, CRG 910551. Moreover, Paris W. Vachon was visiting the Nansen Environmental

and Remote Sensing Center with financial support from the Norwegian Research Council Visiting Research Fellowship and Canada Centre for Remote Sensing. We thank Anita Samuel for processing the ship ADCP and Seasoar data.

References

Alpers, W. R., Theory of radar imaging of internal waves, *Nature*, *314*, 245–247, 1985.

Alpers, W. R., and H. Huhnerfuss, The damping of ocean waves by surface films: A new look at an old problem, *J. Geophys. Res.*, *94*, 6251–6266, 1989.

Askari, F., G. L. Geernaert, W. C. Keller, and S. Raman, Radar imaging of thermal fronts, *Int. J. Remote Sens.*, *14*, 275–294, 1993.

Attema, E., The ERS-1 geophysical validation programme for wind and wave data products, in *Proceedings of ERS-1 Geophysical Validation*, *ESA Publ. WPP-36*, edited by M. Wooding, Eur. Space Agency, Paris, 1992.

Beal, R. C., P. S. DeLeonibus, and I. Katz, (Eds.), *Spaceborne Synthetic Aperture Radar for Oceanography*, 215 pp., John Hopkins Univ. Press, Baltimore, Md., 1981.

Brown, R. A., Surface fluxes and remote sensing of air-sea interactions, in *Surface Waves and Fluxes*, vol. 1, *Current Theory*, edited by G. L. Geernaert and W. J. Plant, Kluwer Academic, Norwell, Mass., 1990.

Donelan, M. A., and W. J. Pierson, Radar scattering and equilibrium ranges in wind-generated waves with application to scatterometry, *J. Geophys. Res.*, *92*, 4971–5029, 1987.

European Space Agency, Proceedings of First ERS-1 Symposium, Space at the service of our environment, *Spec. Publ. ESA SP-359*(1, 2), March 1993.

European Space Agency, Proceedings of Second ERS-1 Symposium, Space at the service of our environment, *Spec. Publ. ESA SP-361*(1, 2), January 1994.

Farge, M., Wavelet transforms and their applications to turbulence, *Annu. Rev. Fluid Mech.*, *24*, 395–457, 1992.

Font, J., et al., Comparison of ERS-1 SAR images of the Western Mediterranean to in situ oceanographic data: PRIM-1 Cruise, in Proceedings of First ERS-1 Symposium, Space at the service of our environment, *Eur. Space Agency Spec. Publ.*, *ESA SP-359*(2), 883–887, March 1993.

Fu, L. L., and B. Holt, Seasat views oceans and ice with synthetic aperture radar, *Publ. 81-120*, 200 pp., Jet Propul. Lab., Pasadena, Calif., 1982.

Fu, L. L., and R. H. Stewart, Some examples of detection of oceanic mesoscale eddies by the Seasat synthetic aperture radar, *J. Geophys. Res.*, *88*, 1844–1852, 1983.

Gower, J. F. R., Wind and surface features in SAR images: The Canadian program, in Proceedings of First ERS-1 Symposium, Space at the service of our environment, *Eur. Space Agency Spec. Publ.*, *ESA SP-359*(1), 101–106, March 1993.

Hasselmann, K., R. K. Raney, W. Plant, W. Alpers, R. A. Shuchman, D. Lyzenga, C. L. Rufenach, and M. F. Tucker, Theory of synthetic aperture radar ocean imaging: A MARSEN view, *J. Geophys. Res.*, *90*, 4659–4686, 1985.

Haugan, P. M., G. Evensen, J. A. Johannessen, O. M. Johannessen, and L. H. Pettersson, Modeled and observed mesoscale circulation and wave-current refraction during the 1988 Norwegian Continental Shelf Experiment, *J. Geophys. Res.*, *96*, 10,487–10,506, 1991.

Johannessen, J. A., E. Svendsen, S. Sandven, O. M. Johannessen, and K. Lygre, Three-dimensional structure of mesoscale eddies in the Norwegian Coastal Current, *J. Phys. Oceanogr.*, *19*, 3–19, 1989.

Johannessen, J. A., R. A. Shuchman, O. M. Johannessen, K. L. Davidson, and D. R. Lyzenga, Synthetic aperture radar imaging of upper ocean circulation features and wind fronts, *J. Geophys. Res.*, *96*, 10,411–10,422, 1991.

Johannessen, J. A., R. A. Shuchman, K. Davidson, Ø. Frette, G. Digranes, and O. M. Johannessen, Coastal ocean studies with ERS-1 SAR during NORCSEX'91, in Proceedings of First ERS-1 Symposium, Space at the service of our environment, *Eur. Space Agency Spec. Publ.*, *ESA SP-359*(1), 113–117, March 1993a.

Johannessen, J. A., L. P. Røed, and T. Wahl, Eddies detected in ERS-1 SAR images and simulated in reduced gravity model, *Int. J. Remote Sens.*, *14*, 2203–2213, 1993b.

Johannessen, J. A., L. P. Røed, O. M. Johannessen, G. Evensen, B. Hackett, L. H. Pettersson, P. M. Haugan, S. Sandven, and R. A. Shuchman, Monitoring and modeling of the marine coastal environment, *Photogramm. Eng. Remote Sens.*, *59*, 351–361, 1993c.

Johannessen, J. A., R. A. Shuchman, and O. M. Johannessen, Mesoscale variability with ERS-1 SAR, in *Oceanographic Application of Remote Sensing*, edited by M. Ikeda and F. Dobson, pp. 27–44, CRC Press, Boca Raton, Fla., 1995.

Krishen, K., Detection of oil spills using a 13.3-GHz radar scatterometer, *J. Geophys. Res.*, *78*, 1952–1964, 1973.

Laur, H., P. Meadows, J. I. Sanchez, and E. Dwyer, ERS-1 SAR radiometric calibration, in SAR Calibration Workshop, *ESA Publ. WPP-048*, Eur. Space Agency, Noordwijk, Netherlands, September 1993.

Lichy, D. E., M. G. Mattie, and L. J. Mancini, Tracking of a warm water ring, in *Spaceborne Synthetic Aperture Radar for Oceanography*, edited by R. C. Beal, P. S. DeLeonibus, and I. Katz, pp. 171–182, Johns Hopkins Univ. Press, Baltimore, Md., 1981.

Liu, A. K., and C. Y. Peng, Waves and mesoscale features in the marginal ice zone, in Proceedings of First ERS-1 Symposium, Space at the service of our environment, *Eur. Space Agency Spec. Publ.*, *ESA SP-359*(1), 343–348, March 1993.

Liu, A. K., C. Y. Peng, and J. D. Schumacher, Wave-current interaction study in the Gulf of Alaska for detection of eddies by synthetic aperture radar, *J. Geophys. Res.*, *99*, 10,075–10,085, 1994a.

Liu, A. K., C. Y. Peng, and T. J. Weingartner, Ocean-ice interaction in the marginal ice zone using synthetic aperture radar imagery, *J. Geophys. Res.*, *99*, 22,391–22,400, 1994b.

Lyzenga, D. R., Interaction of short surface and electromagnetic waves with ocean fronts, *J. Geophys. Res.*, *96*, 10,765–10,772, 1991.

Marr, D., and E. Hildreth, Theory of edge detection, *Proc. R. Soc. London B*, *207*, 187–217, 1980.

Nilsson, C. S., and P. C. Tildesley, Imaging of oceanic features by ERS 1 synthetic aperture radar, *J. Geophys. Res.*, *100*, 953–967, 1995.

Nilsson, C. S., P. C. Tildesley, and J. Petersen, Mapping of the East Australian current with the ERS-1 SAR and shipborne studies, in Proceedings of First ERS-1 Symposium, Space at the service of our environment, *Eur. Space Agency Spec. Publ.*, *ESA SP-359*(1), 95–100, March 1993.

Scott, J. C., Surface films in oceanography, *ONRL Workshop Rep. C-11-86*, pp. 19–34, Off. of Nav. Res., London, 1986.

Stoffelen, A., and D. L. T. Anderson, Wind retrieval and ERS-1 scatterometer backscatter measurements, *Adv. Space Res.*, *13*, 553–560, 1993.

Tilley, D. G., and R. C. Beal, ERS-1 and Almaz ocean wave imaging over the Gulf Stream and Grand Banks, in Proceedings of First ERS-1 Symposium, Space at the service of our environment, *Eur. Space Agency Spec. Publ.*, *ESA SP-359*(2), 729–734, March 1993.

Vesecky, J. F., and R. H. Stewart, The observations of ocean surface phenomena using imagery from the Seasat synthetic aperture radar: An assessment, *J. Geophys. Res.*, *87*, 3397 3430, 1982.

Vesecky, J. F., E. S. Kasischke, and R. A. Shuchman, Marine microlayer effects on the observations of internal waves by SAR, internal report, 65 pp., Environ. Res. Inst. of Mich., Ann Arbor, 1986.

Vogelzang, J., G. J. Wensink, M. W. A., van der Kooij, and R. van Swol, Mapping of sea bottom topography with ERS-1 C-band SAR, in Proceedings of Second ERS-1 Symposium, Space at the service of our environment, *Eur. Space Agency Spec. Publ.*, *ESA SP-361*(2), 945–948, January 1994.

Wright, J. W., Detection of ocean waves by microwave radar: The modulation of short gravity-capillary waves, *Boundary Layer Meteorol.*, *13*, 87–105, 1978.

Wu, J., Effects of atmospheric stability on ocean ripples: A comparison between optical and microwave measurements, *J. Geophys. Res.*, *96*, 7265–7269, 1991.

G. Digranes, Nansen Environmental and Remote Sensing Center, Edvard Griegsvei 3a, 5037 Bergen, Norway.

J. A. Johannessen, European Space Agency, European Space Research and Technology Centre, Postbus 299, 2200 AG Noordwijk, Netherlands. (e-mail: jjohannc@jw.estec.esa.nl)

O. M. Johannessen, Nansen Environmental and Remote Sensing Center, Geophysical Institute, University of Bergen, Edvard Griegsvei 3a, 5037 Bergen, Norway.

D. R. Lyzenga, R. A. Shuchman, and C. Wackerman, Environmental Research Institute of Michigan, P.O. Box 134001, Ann Arbor, MI 48107.

P. W. Vachon, Canada Centre for Remote Sensing, 588 Booth Street, Ottawa, Ontario, Canada K1A 0Y7.

(Received March 14, 1995; revised July 19, 1995;
accepted July 27, 1995.)